Numerical investigation of aerodynamic droplet breakup in a high temperature gas environment

George Strotos[1,a,*], Ilias Malgarinos[1,b], Nikos Nikolopoulos[1,c], ManolisGavaises[1,d]

[1]School of Engineering and Mathematical Sciences, City University London, Northampton Square, EC1V 0HB, London, UK

[a] George.Strotos.1@city.ac.uk

[b] Ilias.Malgarinos.1@city.ac.uk

[c] Nikolaos.Nikolopoulos.1@city.ac.uk

[d] M.Gavaises@city.ac.uk

[*]Corresponding author

Abstract

The Navier-Stokes equations, energy and vapor transport equations coupled with the VOF methodology and a vaporization rate model are numerically solved to predict aerodynamic droplet breakup in a high temperature gas environment. The numerical model accounts for variable properties and uses an adaptive local grid refinement technique on the gas-liquid interface to enhance the accuracy of the computations. The parameters examined include Weber (*We*) numbers in the range $15-90$ and gas phase temperatures in the range $400-1000K$ for a volatile n-heptane droplet. Initially isothermal flow conditions are examined in order to assess the effect of Weber (*We*) and Reynolds (*Re*) number. The latter was altered by varying the gas phase properties in the aforementioned temperature range. It is verified that the *We* number is

23 the controlling parameter, while the *Re* number affects the droplet breakup at low *We* number

24 conditions. The inclusion of droplet heating and evaporation mechanisms has revealed that

25 heating effects have generally a small impact on the phenomenon due to its short duration

26 except for low *We* number cases. Droplet deformation enhances heat transfer and droplet

27 evaporation. An improved 0-D model is proposed, able to predict the droplet heating and

28 vaporization of highly deformed droplets.

29 **Keywords:** droplet breakup; VOF; heating; evaporation

30

31 **1 Introduction**

32 Droplet breakup and evaporation are important physical processes controlling the efficiency of

33 combustion systems; they are also realised in medical and agricultural applications among

34 others. Due to their importance they have attracted the scientific interest; but generally they

35 have been studied independently. The droplet breakup has been addressed (selectively) in

36 review studies as in [1, 2] and droplet evaporation in the review articles by [3, 4] as also in

37 textbooks like [5, 6] among many other.

38 The aerodynamic droplet breakup induced by an initial relative velocity $U_{rel,0}$ between the

39 droplet and the ambient gas is characterized by different breakup modes depending on the

40 relative strength of the forces acting on the droplet. For a certain configuration, increasing the

41 relative droplet-gas velocity results in different breakup regimes namely a) the bag breakup, b)

42 the transitional or multimode breakup (including the bag-stamen, dual-bag and plume/shear

43 regimes), c) the sheet-thinning breakup termed also sheet-stripping or shear breakup and d) the

44 catastrophic breakup. A qualitative description of these breakup regimes can be found in the

45 aforementioned review studies for droplet breakup as in Guildenbecher et al. [1] among many

46 others. Except for the drop-gas relative velocity, other important parameters affecting the

2

aerodynamic droplet breakup are the material (gas and liquid) properties and the droplet dimensions. All these can be grouped into dimensionless numbers, namely the Weber number (*We*), the Reynolds number (*Re*), the Ohnesorge number (*Oh*), the density ratio (ε) and the viscosity ratio (*N*), while under certain flow conditions the Mach number and the turbulence levels may also become important:

$$We = \frac{\rho_g U_{rel,0}^2 D_0}{\sigma} \quad Re = \frac{\rho_g U_{rel,0} D_0}{\mu_g} \quad Oh = \frac{\mu_l}{\sqrt{\rho_l \sigma D_0}} \quad \varepsilon = \frac{\rho_l}{\rho_g} \quad N = \frac{\mu_l}{\mu_g} \tag{1}$$

Experiments have shown that the *We* number is the most influential parameter and thus, most studies aim to define the critical *We* number leading to the different breakup regimes. The critical *We* is mainly a function of the *Oh* number and increases for high viscosity liquids (*Oh*>0.1); the effect of the rest of the dimensionless numbers is not yet quite clear since the majority of the experimental studies have examined relatively high *Re* numbers and density ratios, above 1000 and 600 respectively; a few exceptions examined 500<*Re*<1000 and 80<ε<200 [7, 8].

For the non-dimensionalisation of time, the shear breakup timescale t_{sh} proposed by Nicholls & Ranger [9] is widely used:

$$t_{sh} = \frac{D_0}{U_{rel,0}} \sqrt{\varepsilon} \tag{2}$$

Several experimental studies have investigated the aerodynamic droplet breakup by using the shock tube and the continuous air jet flow techniques (see details in [1] among others). Krzeczkowski [10] was one of first who presented a detailed breakup map in the *We-Oh* plane followed later by the studies of Hsiang & Faeth [11-13] who extended it to higher *Oh* numbers up to 560. Subsequent experimental studies aimed to clarify the physical mechanisms behind the breakup regimes [7, 8, 14] and provided useful information regarding the critical *We* numbers leading to different breakup regimes [15, 16], the temporal properties and the size

3

68   distribution of the child droplets after the parent droplet disintegration [15, 17] and the gas flow

69   structure during droplet breakup [18].

70   Generally, there is a scattering of the experimental data which is probably due to the variety of

71   the experimental techniques used and the experimental uncertainties. Complimentary to the

72   experimental techniques, a large number of numerical works have been performed to enlighten

73   the complicated breakup phenomenon such as those of [19-23]. These studies examined the

74   isothermal droplet breakup in 2D and 3D computational domains and provided insight into the

75   physics behind droplet breakup [19, 20, 22, 23], the effect of parameters other than the *We*

76   number [19] (Re number, density and viscosity ratio), the droplet drag coefficient [21, 23] and

77   the size distribution of droplets after breakup [23].

78   Regarding the evaporation modelling, several simplified 0-D and 1-D models have been

79   proposed to predict the evaporation of isolated spherical droplets. Starting from the classical

80   "D^2-law" of Godsave [24] and Spalding [25], various approaches have been proposed to include

81   the transient droplet heating by prescribing the internal temperature distribution as in [26-31]

82   and the Stefan flow effects as in Abramzon & Sirignano [28] and Yao et al. [32]. The

83   performance of these models was assessed in comparative studies such as those of [33-36] and

84   defined their range of applicability. These models are restricted to spherical droplets and only

85   few exceptions [37-40] have investigated the evaporation of deformed droplets (mainly the

86   oscillatory deformation). Apart from the simplified models which are suitable for the stochastic

87   prediction of the spray performance in Lagrangian models due to their simplicity and reduced

88   computational cost, detailed CFD models [41-44] for single component evaporation and [45-

89   48] for multicomponent droplet evaporation, have been used to give insight on the physical

90   mechanisms occurring during droplet evaporation by solving both the liquid and the gas phase.

91   The coupled problem of droplet breakup and droplet evaporation has not yet been studied

92   thoroughly; only a few CFD studies have examined the heating and evaporation of deformed

93   droplets at low *We* numbers. Haywood et al [49, 50] were one of the first who examined the

94   evaporation of deformed droplets. They used an adaptive grid fitted to the droplet surface which

95   could predict its deformation but not the breakup. They examined n-heptane droplets in a high

96   temperature gas (1000K) at moderate *Re* numbers (10<*Re*<100) and low *We* numbers (*We*<10).

97   They showed that when using a volume-equivalent diameter, the quasi-steady correlations for

98   the Nusselt (*Nu)* and Sherwood (*Sh)* numbers can also be used for droplets under steady or

99   unsteady (oscillatory) deformation. On the contrary, the drag coefficient is influenced by the

100   droplet shape and it is a function of *Re* and *We* numbers; if the instantaneous dimensionless

101   droplet frontal area is known, then the classical 0-D correlations can be used by multiplying

102   them with this parameter. Mao et al. [51] used a body fitted grid to study the mass transfer of

103   deformed droplets for *We*<8. They concluded that the Peclet (*Pe*) number followed by the *Re*

104   number are the controlling parameters, while the *We* number has a small impact on the droplet

105   evaporation rate evolution only at very high *Pe* numbers. Hase & Weigand [52] used a 3D VOF

106   methodology to study the heat transfer enhancement (without evaporation) due to the

107   deformation of hot droplets carried by a colder air stream at high Reynolds numbers

108   (360<*Re*<853) and *We*<11. They found a significant dependency of *Nu* on *We* number at the

109   highest *Re* number case, but to our opinion this conclusion might has been affected by the fact

110   that the heat transfer coefficient was estimated by using the surface area of a sphere. They have

111   also shown that the heat transfer increases not only due to the droplet oscillatory motion but

112   also due to the larger surface area of the deformed droplet; in addition, the transient *Nu* number

113   at the beginning of the simulation is much higher compared to the steady-state *Nu* number given

114   by classical correlations. In a follow-up study, the same group [53] included evaporation in

115   their model (as in [44]) and examined the coupled problem of droplet deformation and

116   evaporation. They studied cases including initially spherical or deformed droplets and also

117   isothermal and evaporating cases with the presence of heat transfer from the hot ambient air.

118   The dimensionless numbers examined were in the range of 173<*Re*<347 and 2.3<*We*<7.8. They

119   found that the flow field inside the droplets is affecting the droplet heating; the oscillatory

120 droplet movement causes a "sucking" of hotter fluid from the droplet surface towards its centre.

121 They have also identified large temperature differences along the droplet surface which

122 influences the mass transfer and may induce a thermo-capillary flow; however this mechanism

123 was not modelled. Cerqueira et al. [54] studied the interfacial heat and mass transfer in spherical

124 and deformed rising bubbles for $Re<80$ with the VOF methodology. It was shown that the shape

125 distortion results in decrease of the transfer coefficient and increase of the interfacial area,

126 compensating the effect on the total interfacial flow; the latter becomes dominant in highly

127 distorted particles.

128 The present numerical work aims to fill the gap in literature concerning the coupled problem of

129 droplet breakup in a high temperature environment accounting for the droplet heating and

130 evaporation. The effect of heating and evaporation on droplet breakup is quantified by

131 comparing non-isothermal against isothermal cases at the same flow conditions. The numerical

132 model employs the VOF methodology coupled with the solution of the energy equation, while

133 a local evaporation model is used, which is independent of the droplet shape. The following

134 sections include initially a brief description of the numerical methodology and the cases

135 examined, followed by the results under isothermal and evaporating conditions. The

136 conclusions of the present work are summarized at the end.

137

138 ## 2　Numerical model and methodology

139 The numerical model solves the Navier-Stokes equations in a 2D axisymmetric domain and

140 uses the VOF methodology to track the liquid-gas interface. To account for the droplet heating

141 and evaporation, the energy and vapour transport equations are also solved, while the

142 evaporation mass flux is obtained by using a local evaporation model independent of the

143 interface shape, assuming that the computational cells at the liquid-gas interface are saturated.

144 For the non-isothermal cases, the pure species properties are assumed to be a function of

145   temperature according to [55, 56] and the gas mixture properties are taken as mass-averaged

146   based on the vapour concentration assuming incompressible ideal gas.

147   The complete set of the equations solved were in detail presented in Strotos et al. [57] and will

148   not be repeated here. The model has already been validated against a wide range of cases and

149   thus it can be considered to be reliable. These include the motion of a free falling droplet in

150   Malgarinos et al. [58], the aerodynamic breakup of droplets in Strotos et al. [59, 60], the

151   evaporation of single- and multi-component droplet in a high temperature environment in

152   Strotos et al. [57], but also droplet impact onto a solid substrate in Malgarinos et al. [61].

153   The platform provided by the CFD tool ANSYS FLUENT v14.5 [62] was utilized for solving

154   numerically the flow equations; the implicit VOF solver was adopted, which has a robust

155   behavior and allows for higher timesteps when compared to the explicit solver. A number of

156   User Defined Functions (UDFs) were developed and implemented allowing for simulation of

157   the droplet vaporization during their break-up process. These include (apart from the

158   evaporation model and species properties) an automatic local grid refinement technique [61,

159   63], a sharpening algorithm [59] and also the implementation of variable timestep based on a

160   Courant number (C) equal to 0.5 at the interface region; this is a minor change relative to our

161   previous work reported in Strotos et al. [59, 60], in which the Courant number was calculated

162   in the whole computational domain rather than on the interface. The following discretization

163   methods have been utilized: the Compressive discretization scheme for the interface tracking,

164   the Second Order Upwind (SOU) discretization for the momentum and energy equations, the

165   First Order Upwind (FOU) for the species transport equations (a higher order scheme may lead

166   to divergence), the Body Force Weighted (BFW) pressure interpolation scheme, the PISO

167   algorithm for the pressure-velocity coupling and the Bounded Second Order Implicit (BSOI)

168   formulation for the temporal discretization (see details in our previous works as also in [62]).

169   Finally, for the implementation of the surface tension force in the momentum equations, the

170   Continuum Surface Stress (CSS) model by Lafaurie et al. [64] was used in order to include the

7

171 effect of the thermo-capillary flow due to the variation of the surface tension coefficient along

172 the interface. The numerical settings used for the simulations are summarized in Table 1.

173

174 Table 1: Numerical settings used for the simulations.

Equation	Discretization scheme
VOF	Compressive
Momentum	SOU
Energy	SOU
Species	FOU
pressure interpolation scheme	BFW
Pressure-velocity coupling	PISO
time discretization	BSOI

175

176

177

3 Results and discussion

3.1 Cases examined and numerical setup

180 The cases examined involve a small (D_0=100μm) volatile n-heptane droplet subjected to a step

181 change of the gas phase velocity. The droplet has an initial temperature of T_0=300K which

182 corresponds to Oh=0.01 and ensures that the breakup regime is not depending on the Oh

8

183   number; the *Oh* number was kept constant for all cases examined. The ambient pressure is

184   atmospheric which ensures the validity of the evaporation model and no high pressure

185   modifications were required. The gas phase velocity is modified so as to achieve *We* numbers

186   in the range 15 up to 90, while the free stream temperature is varying in the range of 400-

187   1000K; for a given temperature, the gas properties are first calculated and then the gas phase

188   velocity is obtained from the *We* number definition. Altering the free stream temperature results

189   in density and viscosity ratios in the range of ε=770-1926 and *N*=9.1-16.5, respectively, which

190   according to Aalburg [65] are high enough (well above ε>32) to affect the breakup outcome.

191   Note also that the critical n-heptane temperature is 540K and the present model has been already

192   validated from the authors against supercritical temperatures in Strotos et al. [57].

193   The aforementioned combinations of *We* number and free stream temperatures, led to high free-

194   steam velocities in the range of 57-223m/s, but the compressibility effects are negligible since

195   the maximum Mach number is 0.35 (observed for *We* =90). In all cases the *Re* number is below

196   400 which ensures that the flow remains laminar and the axisymmetric solution is applicable

197   [5, 66]. Nevertheless, in the parametric study conducted in Strotos et al. [60] with the 2D

198   axisymmetric model, the *Re* numbers examined were much higher without affecting the

199   qualitative model performance.

200   A complete list of the cases examined is shown in Fig. 1 in the *We-T_∞* plane and the *We-Re*

201   plane. For the isothermal cases, the energy equation and the evaporation source terms were not

202   accounted for and the species properties were kept constant at their reference temperature

203   values, i.e. at T_0=300K for the liquid droplet and at T_∞ for the surrounding air; namely,

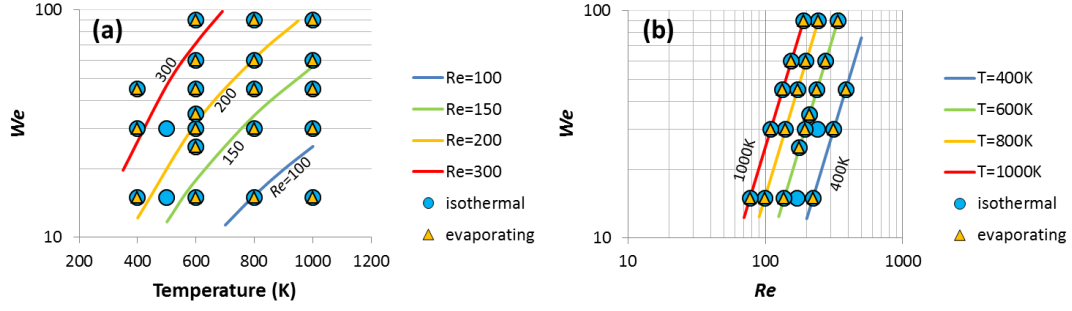204   isothermal runs correspond to a parametric study for the effect of *We* and *Re* numbers.

205

Fig. 1: Cases examined in (a) the We-T_∞ plane and (b) the We-Re plane.

206

207

208 Regarding the computational domain and the boundary conditions, these are the same as in

209 Strotos et al. [59, 60]. Briefly, the droplet is initially motionless and it is subjected to a step

210 change of the gas phase velocity. The grid is moving with the average droplet velocity and

211 upstream the droplet a fixed absolute velocity and temperature is applied (Dirichlet boundary

212 condition), while downstream a zero first gradient boundary for all variables is used. The

213 unstructured grid has a density of 192 cells per radius (cpR) at the interface region and it is fine

214 enough to resolve the boundary layers. More specifically, in Feng & Michaelides [67] it is

215 stated that the hydrodynamic boundary layer thickness is proportional to $Re^{-1/2}R$; for Re=400 it

216 has a thickness of $0.05R$. For the highest Re number examined here, there are 9-10

217 computational cells inside the boundary layer region, which can be considered a realistic grid

218 resolution for VOF simulations suitable for the present runs.

219

220 3.2 Isothermal cases

221 3.2.1 General breakup behaviour

222 The results obtained for the droplet shapes assuming isothermal flow conditions and constant

223 properties are shown in Fig. 2. The droplet shapes drawn in black correspond to time intervals

10

224 of 0.5t_{sh} (i.e. 0.0, 0.5, 1.0, 1.5, 2.0t_{sh}) and the droplets drawn in red correspond to intermediate

225 instances i.e. 0.75, 1.25, 1.75, 2.25t_{sh} (the time instant of 0.25t_{sh} has been omitted); the last

226 droplet shape corresponds to the instant of breakup. For a direct correspondence to Fig. 1b, the

227 *We* number increases from bottom to top and the gas phase temperature from right to left. With

228 this arrangement, the *Re* number increases from bottom to top and from left to right. These runs

229 verify that the *We* number is the controlling parameter. Increasing the *We* number results in

230 different breakup regimes, namely bag breakup for *We*=15, multimode breakup for *We*=30-60

231 and sheet thinning breakup for *We*=90. Nevertheless, the transition between the multimode and

232 the sheet-thinning breakup is not quite clear verifying that breakup is a continuous process [1];

233 this is also affected by the low *Re* numbers examined. We have assumed that *We*=90

234 corresponds to sheet-thinning breakup due to the fact that the droplet breaks up earlier, before

235 it is subjected to a high stretching. A false three-dimensional representation of the cases
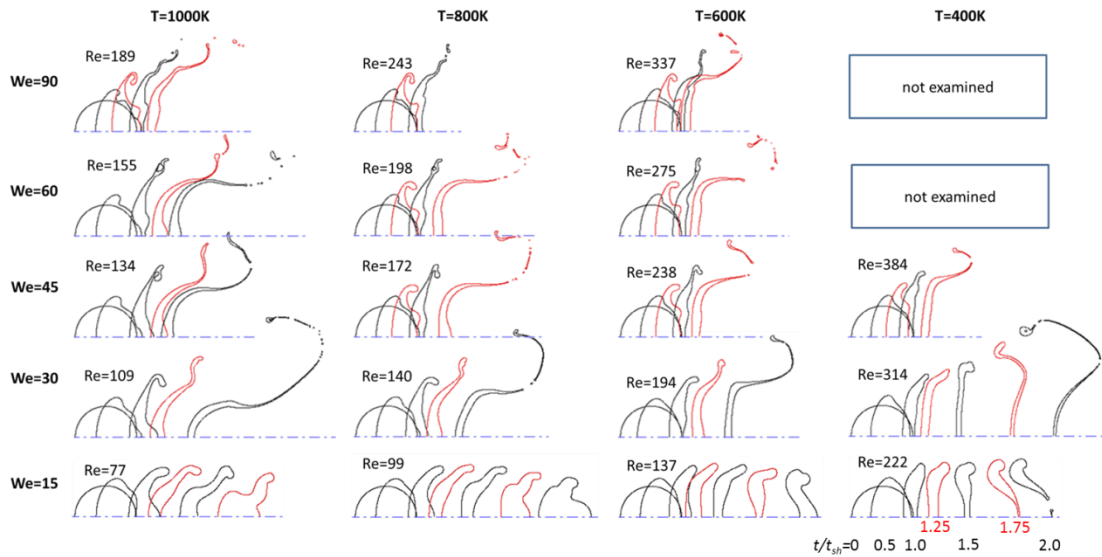
236 corresponding to T_∞=400K is shown in Fig. 3.

237

239 Fig. 2: Droplet shapes for the isothermal runs. The *Re* number increases from bottom to top and

240 from left to right. The droplet shapes drawn black (see the online version) correspond to time

11

241   intervals of $0.5t_{sh}$ and the droplet shapes drawn red correspond to representative intermediate

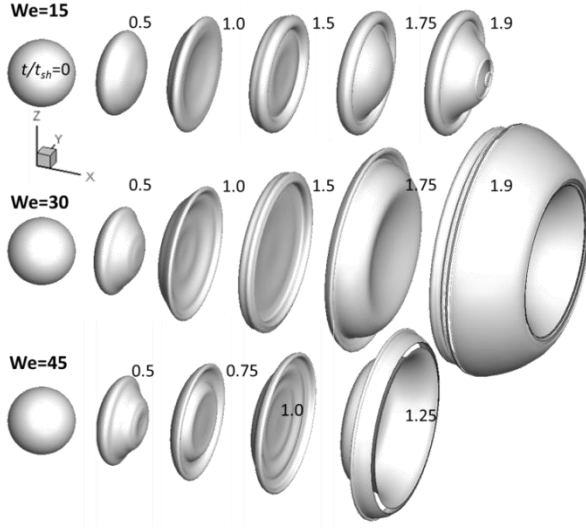242   instances of $0.25t_{sh}$. The last droplet shape corresponds to the instant of breakup.

243

244

245   Fig. 3: Three-dimensional representation of the droplet shape evolution at three different *We*

246   numbers examined for the isothermal cases corresponding to T_∞=400K.

247

248   As already stated in section 3.1, the density and the viscosity ratios examined are high enough

249   so that do not affect the results; thus, the *Re* number is the remaining parameter affecting the

250   outcome for the isothermal runs. Earlier numerical studies have shown that there is a

251   dependency on *Re* number for *Re*<100 [65]. The present simulations for 77<*Re*<385 have

252   shown that decreasing the *Re* number does not alter the breakup outcome, but results in a

253   slightly higher deformation of the liquid structure for intermediate *We* numbers in the range 30-

254   60. On the other hand, the effect of *Re* number at the lowest *We* number case of *We*=15 should

255   be emphasized. It is clear that there is a critical *Re* number between 137 and 170 (the latter was

256   obtained for T_∞=500K), below which no breakup is observed; it can be assumed that for *We*=15

257   and *Oh*=0.01 the critical *Re* number is 155 (an average of the aforementioned numbers). This

258 fact was also observed in the numerical work of Han & Tryggvason [19] and it is also stated in

259 the review article of Guildenbecher et al. [1] that there is a dependency on *Re* number in the

260 bag breakup regime. In any case, one should have in mind that the 2D axisymmetric simulations

261 performed in this study ignore three-dimensional effects which probably alter the phenomenon

262 at the last stages near the breakup.

263 The predicted dimensionless breakup time (the so-called "initiation time") for the isothermal

264 cases is shown in Fig. 4, along with the corresponding experimental correlations given by Pilch

265 & Erdman [68] and Dai & Faeth [15]. The temperatures appearing in the legend of Fig. 4

266 correspond to the hypothetical free stream temperature at which the gas phase properties were

267 calculated; so for the same *We* number, a different temperature indicates a different *Re* number.

268 The predicted breakup time lies between the experimental correlations and correctly predicts

269 the faster breakup with increasing *We* number, while there is only a weak dependency on *Re* at

270 low *We* numbers. However, the experimental correlations are subjected to several uncertainties

271 regarding the estimation of the initiation time as Khosla & Smith [20] stated; moreover, our

272 estimation of the breakup time is subjected to errors in the order $0.05 t_{sh}$ (2.5-5%) since this is

273 manually obtained by examining post-processed images. Despite the aforementioned

274 uncertainties, the general trend is correctly predicted and a best fit curve representing our results

275 is $t_{br}/t_{sh}=6.06We^{-0.4}$. Generally the duration of the phenomenon is short and in dimensional units
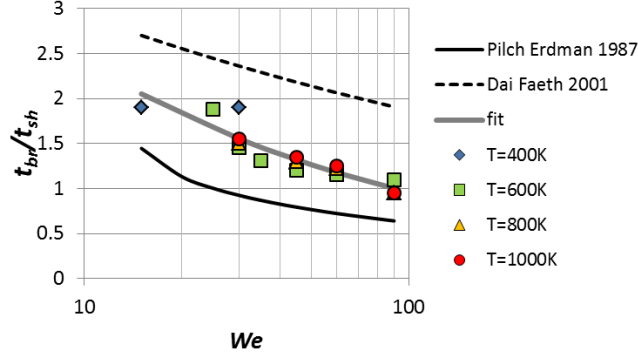
276 it lasts 20-100μs for the examined cases.

277

278

279   Fig. 4: Predicted dimensionless breakup time for the isothermal cases.

280

3.2.2 Measured quantities during breakup

282   The temporal evolution of the droplet's cross-stream diameter (D_c) and velocity are given in

283   Fig. 5 (a) and (b) respectively for selected cases corresponding to bag, transitional and sheet-

284   thinning breakup. The axes of the graphs have been non-dimensionalized as in Dai & Faeth

285   [15], thus allowing for a direct comparison with their experimental data and showing a good

286   qualitative agreement; here u represents the instantaneous droplet velocity and U the free stream

287   gas phase velocity. As seen, the droplet's cross-stream diameter after a short non-deforming

288   period of approximately $0.3t_{sh}$ starts to increase almost linearly with time, in agreement with

289   the experimental findings of Cao et al. [16]. Nevertheless, the present results show a slightly

290   different behaviour at the later stages of the bag breakup in which the cross-stream diameter

291   stabilizes near its maximum. This is attributed to the low Re number case, since our simulations

292   for high Re numbers in [60] shows a continuously increasing deformation. Regarding the

293   droplet velocity depicted in Fig. 5b, this increases continuously with time but with a

294   progressively decreasing rate and agrees with the experimental data of Dai & Faeth [15].
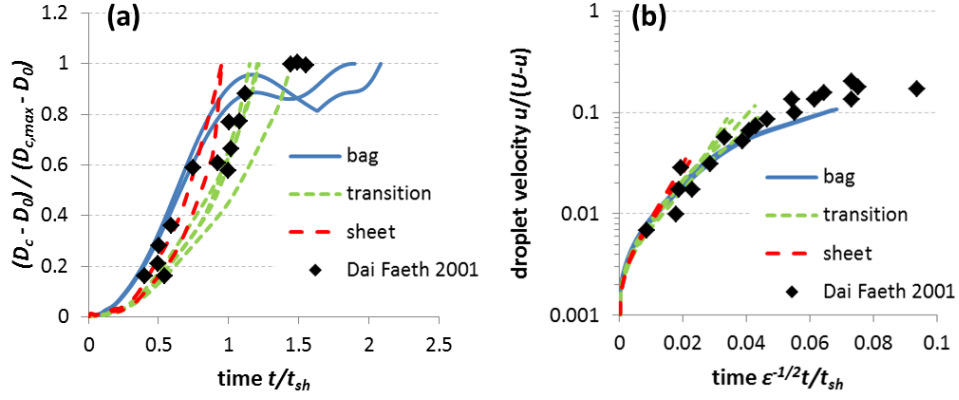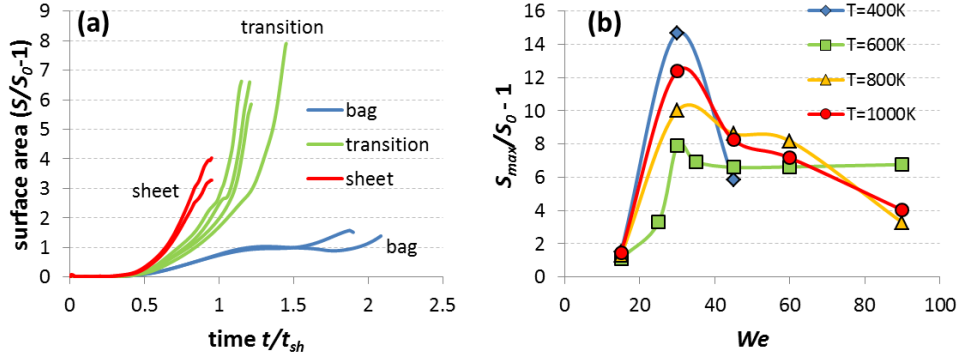
295

14

Fig. 5: Temporal evolution of (a) droplet's cross-stream diameter and (b) droplet's velocity for selected isothermal cases.

The droplet's surface area (S) is of interest due to its importance in combustion systems; moreover, it is a quantity which is difficult to measure experimentally. This parameter is shown in Fig. 6a for selected cases corresponding to the breakup regimes examined. The surface area is non-dimensionalized with that of a sphere (S_0) having the same volume. As seen in Fig. 6a, the droplet surface area after the initial non-deforming period starts to increase with a fast rate, exhibiting dimensionless deformation rates of the order 1.3-8, which increases with increasing We number; this behaviour is in accordance with the findings of Han & Tryggvason [19]. For the bag breakup cases (We=15), the droplet surface area increases with an almost linear way (deformation rate $\sim$1.3) and at the time instant of breakup it is approximately equal to $2.5S_0$. For the transitional breakup cases (We=30-60), the droplet surface area exhibits a different behaviour characterised by a higher rate of deformation. After the initial non-deforming period the droplet surface area increases exponentially and exhibits a high stretching, exceeding values of $7S_0$. Finally, the sheet-thinning breakup cases exhibit even higher rate of deformation, but the droplet breaks up earlier and thus the final droplet deformation is lower than that of the transitional case at the instant of breakup.

15

315

316

317 Fig. 6: (a) Temporal evolution of the dimensionless droplet surface area for selected isothermal

318 cases and (b) maximum surface area as a function of *We* number.

319

320 In the absence of a conservation law for the surface area evolution, the temporal evolution of

321 droplet surface area can be approximated with the fitting curve of Equation 3 and the

322 coefficients c_1 and c_2 imply that the rate of deformation increases with increasing *We* and

323 decreasing *Re* number; Equation 3 is valid for $t<t_{sh}$ and the entire range of the isothermal

324 conditions examined, i.e. $15<We<90$, $77<Re<385$. It has to be noted that the selection of the

325 *sinh* function in Equation 3 was found to be the most suitable choice among many options

326 examined including the polynomial, power and exponential; since *sinh*(0)=0 (which

327 corresponds to an initially spherical droplet), the initial non-deforming period is reasonably

328 well predicted and increases with a progressively faster rate.

$$S/S_0 - 1 = c_1 sinh\left(c_2 \cdot \frac{t}{t_{sh}}\right), \qquad t < t_{sh} \tag{3a}$$

$$c_1 = 0.0082 We^{0.537} \tag{3b}$$

$$c_2 = 5.47 We^{0.136} Re^{-0.138} \tag{3c}$$

16

329   This curve was obtained by fitting the surface area up to $t=t_{sh}$ since after this time a more

330   complicated function is needed to capture the temporal evolution of the surface area, which

331   may change slope due to the appearance of interfacial instabilities. The fitting curve can be

332   extended up to $t=t_{br}$ (except of the bag breakup cases) to give a rough estimation of the surface

333   area at the instant of breakup. However, our predictions of the surface area at the instant of

334   breakup (see Fig. 6b) have shown that this magnitude is not following a smooth variation when

335   the We and Re numbers are changing, while a local peak at $We=30$ is observed. This is mainly

336   attributed to the error of the estimation of the breakup instant, but also on interfacial instabilities

337   which suddenly alter the rate of deformation. Concluding, Equation 3 should be used with

338   caution for $t_{sh}<t<t_{br}$ and limit the maximum value not to exceed $10\text{-}14 S_0$, since unphysical

339   values may obtained.

340   The drag coefficient of the deformed droplets is of major interest due to its importance in

341   breakup models. There are various approaches to estimate the drag coefficient. Here we have

342   adopted the correlations given in Pilch & Erdman [68]:

$$\frac{X}{D} = \frac{3}{8} C_D \left(\frac{t}{t_{sh}}\right)^2 + B \left(\frac{t}{t_{sh}}\right)^3 \tag{4}$$

$$\frac{u}{U}\sqrt{\varepsilon} = \frac{3}{4} C_D \left(\frac{t}{t_{sh}}\right) + 3B \left(\frac{t}{t_{sh}}\right)^2 \tag{5}$$

$$\frac{du}{dt}\frac{D \cdot \varepsilon}{U^2} = \frac{3}{4} C_D + 6B \left(\frac{t}{t_{sh}}\right) \tag{6}$$

343   These equations (4-6) are valid for gas-droplet systems (i.e. high density ratios ε), while the

344   coefficient B accounts for the changing of the droplet frontal area and the unsteadiness of the

345   drag coefficient (i.e. $B=0$ would denote a sphere at steady state). Pilch & Erdman [68] assumed

346     $C_D=0.5$ which corresponds to the drag coefficient of a solid sphere for incompressible flow and

347   high Re numbers ($Re>1000$), and fitting the droplet displacement data with Equation 4, they

348   obtained a value of B equal to 0.0758. Here a similar approach is adopted, but without a-priori

349   assuming a value for the drag coefficient. The results obtained for C_D and B are shown in Fig.

350   7 versus the Re number. The drag coefficient shown in Fig. 7a decreases with the Re number

351   and it is close to the drag coefficient of a solid sphere [5] and to that of a fluid sphere [67] at an

352   average viscosity ratio of the cases examined. It has to be noted that the case with $We=15$

353   exhibits a higher C_D which is due to the hollow spherical shape of the bag breakup. Regarding

354   the correction coefficient B shown in Fig. 7b, there is a different behaviour depending on the

355   breakup type. Bag breakup is characterized by low B values (~0.07) with a slightly increasing

356   trend with Re number, while the other breakup regimes are characterized by higher B values

357   (0.3-0.4) with a decreasing trend with Re number. A better understanding of the trends for the

358   aforementioned coefficients requires the examination of a wider range of We and Re numbers.
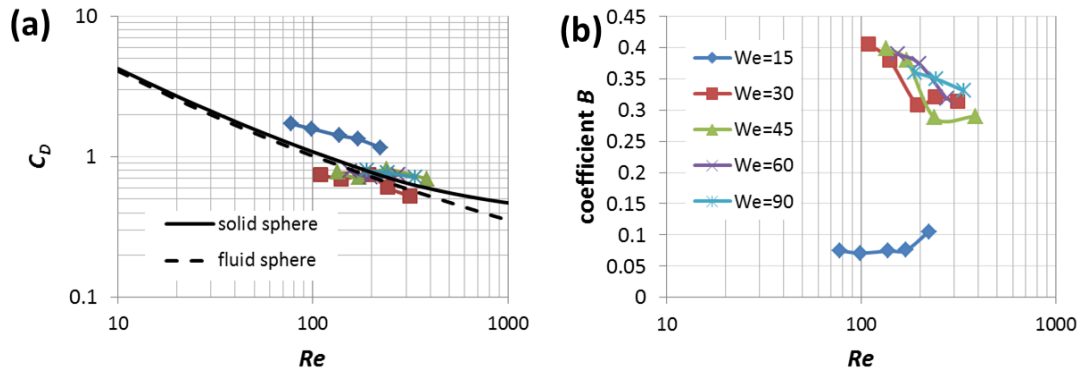
359

360

361   Fig. 7: (a) drag coefficient C_D and (b) coefficient B obtained from curve fitting of the droplet

362   displacement data for the isothermal cases.

363

364   It is also interesting to examine the transient ratio of the instantaneous deforming versus the

365   restorative forces acting on the droplet. Ignoring the viscous forces (since $Oh<0.1$) this ratio

366   represents an instantaneous Weber number We_t (aerodynamic vs surface tension forces) defined

367   with the instantaneous droplet-gas relative velocity $u_{rel,t}$ and the cross-stream diameter $D_{c,t}$ (see

18

368   Equation 7); the instantaneous droplet-gas relative velocity is obtained by subtracting the

369   instantaneous volume averaged droplet velocity from the free-stream gas phase velocity.

$$We_t = \frac{\rho_g u_{rel,t}^2 D_{c,t}}{\sigma} = We_0 \left(\frac{D_{c,t}}{D_0}\right) \left(\frac{u_{rel,t}}{U}\right)^2 \tag{7}$$

370   The predicted transient *We* number based on Equation 7 is plotted in Fig. 8a for selected cases.

371   It is clear that in the cases which lead to breakup, the deformation forces become progressively

372   stronger compared to the restorative forces since We_t increases, while in the non-breakup cases,

373   after reaching a maximum, the deformation forces progressively decrease. Two curves are also

374   shown in Fig. 8a. These arise from Equation 7 evaluated at the instant of breakup by using

375   either the breakup time of Dai & Faeth [15] (abbreviated as D-F 2001), or the correlation of

376   Pilch & Erdman [68] for *Oh*=0.01 (abbreviated as P-E 1987). In both curves the cross-stream

377   diameter and the relative droplet-gas velocity were obtained from the data of [15]; as seen, the

378   predicted breakup falls between these two curves. When the two lines cross, breakup occurs.

379   So, this plot represents a critical instantaneous condition for breakup. The critical instantaneous

380   conditions for various breakup regimes as a function of the *Oh* number are shown in Fig. 8b.

381   This is a qualitative graph obtained by using the breakup time of Pilch & Erdman [68] which

382   accounts for the effect of *Oh* number, typical critical *We* numbers leading to different breakup

383   regimes (12-35 for bag breakup, 35-80 for transitional and 80 for sheet-thinning), as also the

384   dependency of the critical *We* number versus the *Oh* number; $We_{cr}=We_{cr,Oh\rightarrow0}(1+1.077Oh^{1.6})$,

385   *Oh*<10 from [68]. This graph reveals that increasing the *Oh* number (i.e. the viscous forces)

386   requires more time and higher instantaneous aerodynamic forces for breakup to occur;

387   nevertheless, this cannot be verified in the present work since for all cases examined the *Oh*

388   was kept constant to 0.01.

389
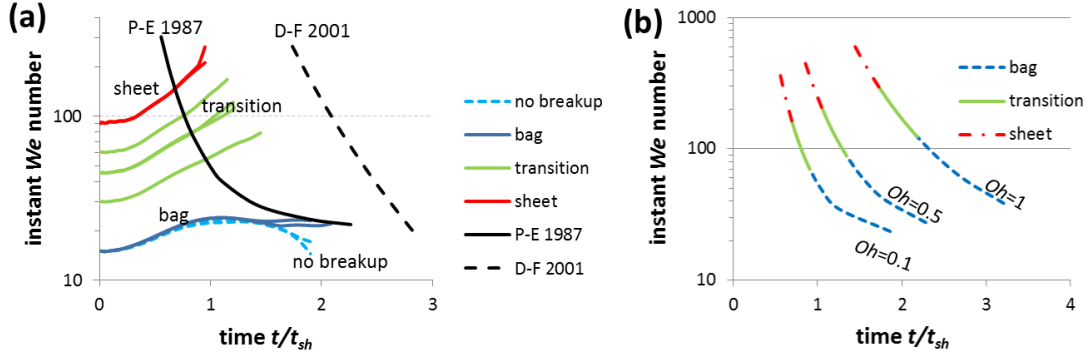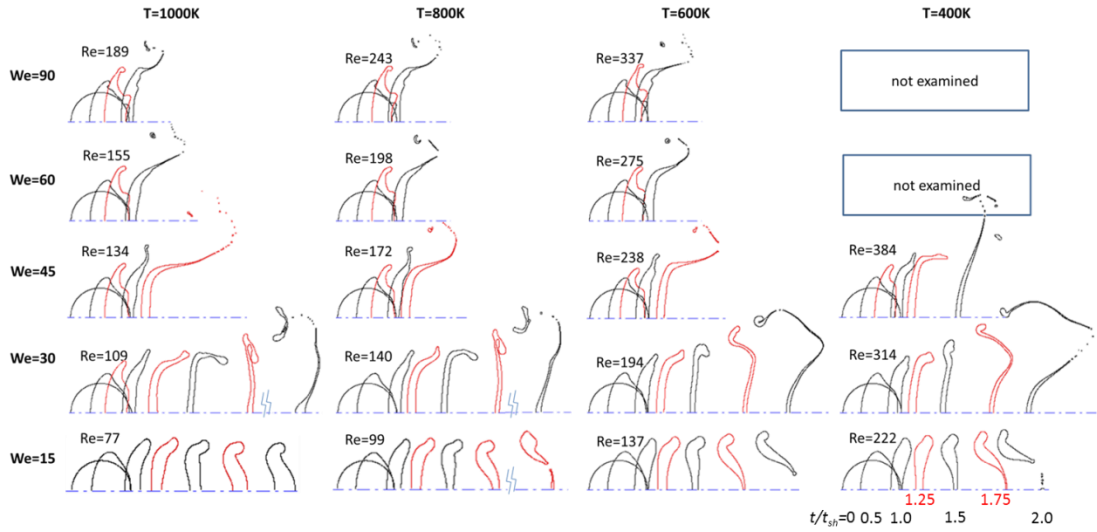
Fig. 8: (a) Predicted instant *We* number for selected isothermal cases and (b) instantaneous critical breakup conditions for various *Oh* numbers.

3.3 Evaporating cases

3.3.1 Hydrodynamic behaviour of the droplet

Focusing now on the cases including droplet heating and evaporation with variable properties, the results obtained for the droplet shapes are shown in Fig. 9 using the same pattern as in Fig. 2. Similar to the isothermal cases, the *We* number is the controlling parameter leading to bag breakup for low *We* numbers and multimode breakup for intermediate *We* numbers (*We*=30-60); moreover, we have assumed that *We*=90 corresponds to the sheet thinning breakup due to the earlier droplet breakup. Compared to the isothermal cases, the droplet heating and evaporation has a minor effect on the droplet breakup for *We*>30, since quite similar droplet shapes were obtained. On the other hand, there is a significant influence for the low *We* number of 15 case in which droplet breakup is observed for a lower *Re* number in-between 77 and 99; it has been assumed that the critical *Re* number is 88 and while in the isothermal cases the critical *Re* was found to be 155. The effect of heating on droplet breakup is that the surface tension coefficient decreases with a subsequent reduction of the restorative forces; these points will be further discussed in the following sections of the paper.

20

409

Fig. 9: Droplet shapes for the evaporating cases. The *Re* number increases from bottom to top and from left to right. The droplet shapes drawn black (see the online version) correspond to time intervals of $0.5t_{sh}$ and the red droplet shapes correspond to representative intermediate instances of $0.25t_{sh}$. The last droplet shape corresponds to the instant of breakup.

Regarding the hydrodynamic characteristics of droplet breakup, it seems that these remain rather unaffected by the droplet heating. The instant of breakup is quite similar in the isothermal and the evaporating cases with an exception for the case (*We, Re, T*)=(15, 99, 800) which requires more time for breakup since it is very close to the "estimated" critical *Re* number of 88 for bag breakup to occur. The maximum surface area and the drag coefficient are within the same range of values as in the isothermal cases, but the coefficient *B* shows a scatter in the evaporating cases; nevertheless it has the same range of values as in the isothermal cases. A comparison of the predictions between the isothermal and the evaporating simulations for the aforementioned quantities is shown in Fig. 10.
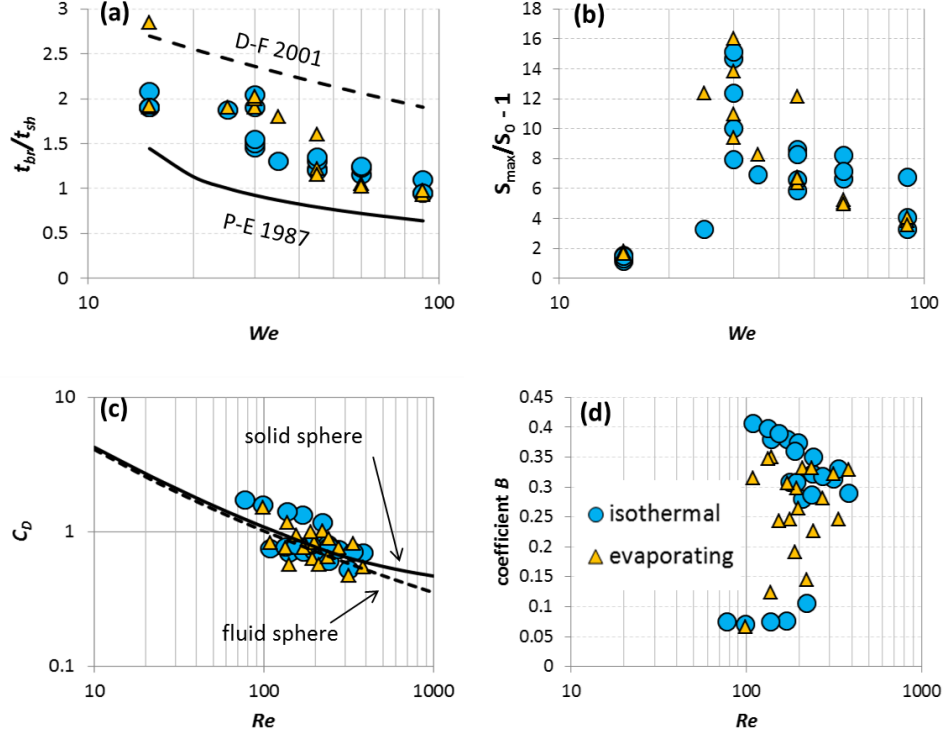
21

Fig. 10: Comparison of the predictions of the isothermal and the evaporating simulations for the (a) breakup instant, (b) maximum surface area, (c) drag coefficient and (d) coefficient B.

3.3.2 Thermal behaviour of the droplet

Turning now to the thermal characteristics of the cases examined, the temporal evolution of the volume averaged droplet temperature T_m and evaporation rate dm/dt are presented in Fig. 11a,b, respectively, for the representative case with $We=30$ and $T_\infty=600K$. In order to assess the effect of evaporation and the effect of the surface area increase, two more cases are presented in Fig. 11, apart from those mentioned in section 3.1. In the first one, the evaporation source terms have been omitted (label "deforming droplet without evaporation") while in the second one, the surface tension coefficient was artificially increased in order to achieve a nearly spherical droplet subjected to small shape oscillations (label "spherical droplet with evaporation"). Comparing the two evaporating cases (deformed and spherical), one can clearly see the effect

22

439   of droplet deformation which increases the total heat transfer to the droplet due to the surface

440   area increase. Comparing the deforming cases with and without evaporation, one can clearly

441   see that evaporation decreases the heat transfer due to the thickening of the boundary layers

442   (Stefan flow) as also due to the fact that a portion of the heat transferred to the droplet is spent

443   for phase change. The evaporation rate in Fig. 11b shows that the droplet deformation results

444   in a more intense increase of the mass transfer from the droplet compared to the spherical

445   droplet case; nevertheless, due to the short duration of the breakup phenomenon, the total

446   evaporated mass is in the range 0.3-2.0% of the initial droplet mass for all cases examined and

447   similarly the volume averaged droplet heat-up is in the range 0.4-7K. Due to the thermal

448   expansion effect, the droplet volume changes less than the droplet mass and it does not exceed
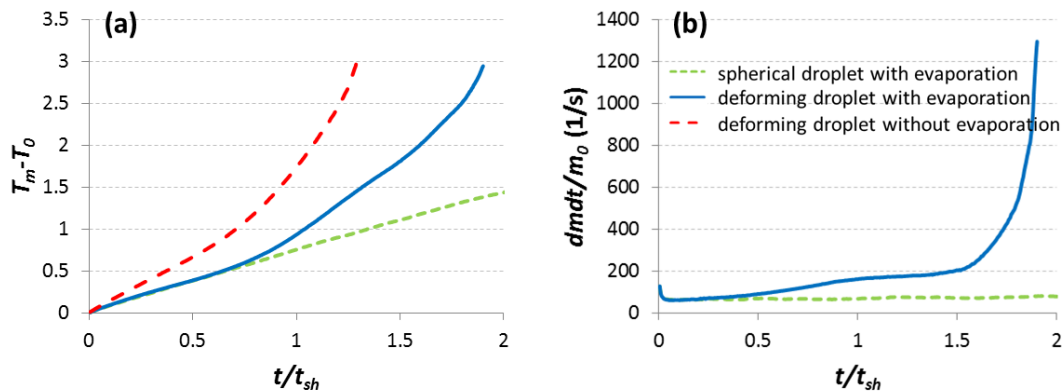
449   1% of the initial volume.

450

451

452   Fig. 11: Temporal evolution of (a) volume averaged droplet temperature and (b) evaporation

453   rate for the case of (We, T_∞)=(30, 600).

454

455   It is also of interest to estimate the Nusselt (Nu) and Sherwood (Sh) numbers for the heat and

456   mass transfer respectively and then use them in simplified 0-D models aiming to predict droplet

457   heating. The Nu and Sh numbers represent the dimensionless temperature and concentration

23

458   gradients respectively at the droplet interface; earlier studies using body-fitted grids [41, 42]

459   estimated them directly by calculating the gradients at the interface. Nevertheless, this is not

460   straightforward within the framework of the VOF simulations, because of the continuous

461   variation of the field magnitudes at the interface region. As a result, the discontinuities of

462   temperature and concentration gradients at the interface region cannot be captured even with a

463   very fine mesh (see also details in [54]). In order to estimate them, a different approach is

464   adopted which is based on 0-D relationships outlined in equations 8-13. These form an

465   enhanced 0-D model which can also estimate the surface temperature through an additional

466   equation relating the droplet surface temperature with its volume averaged one; this was

467   inspired by the work of Renksizbulut et al. [29]:

$$\rho_l V \frac{d(c_{p,l}T_m)}{dt} = S\left(\frac{Nu \cdot k_{g,\infty}}{D_0}(T_\infty - T_s) - \dot{m}''L\right) \tag{8}$$

$$\dot{m} = S\frac{Sh \cdot \rho_{g,\infty}D_{AB,\infty}}{D_0}ln(1 + B_M) \tag{9}$$

$$Nu_l \cdot k_{l,0}\frac{T_s - T_m}{D_0} = Nu \cdot k_{g,\infty}\frac{T_\infty - T_s}{D_0} - \dot{m}''L \tag{10}$$

$$\overline{Nu} = \frac{2 + 1.18Re_\infty^{0.346}Pr_{g,\infty}^{1/3}}{\left(1 + B_{T,\infty}\right)^{0.7}} \tag{11}$$

$$\overline{Sh} = \left(2 + 0.062Re_\infty^{0.915}Sc_{g,\infty}^{1/3}\right)\left(1 + B_{T,\infty}\right)^{0.6} \tag{12}$$

$$\overline{Nu_l} = 53.63 + Re_l/59.62 \tag{13}$$

468   Equation 8 is the overall droplet energy balance; Equation 9 is a commonly used relationship

469   for the evaporation rate and Equation 10 is the heat flux continuity at the droplet's surface, in

470   which Nu_l represents the dimensionless temperature gradient from the liquid side; this equation

471   connects the average droplet temperature T_m with the surface temperature T_s. Using the CFD

472   data for the mean droplet temperature T_m, the spatial average surface temperature T_s and the

473   evaporation rate dm/dt, from equations 8-10, one can solve for Nu, Sh and Nu_l numbers and

474   find their variation with time; a similar concept was used by Hase & Weigand [52] in order to

475   obtain the Nu number but without evaporation. This is shown in Fig. 12 for the case

476    $(We, T_\infty)=(30, 600)$ which can be regarded as representative, since the qualitative characteristics

477   observed apply to all cases examined. The Nu and Sh numbers after a short initial transitional

478   period related to the development of the flow fields around and inside the droplet, remain almost

479   constant with time. The Nu_l number has a more unsteady character. It exhibits a larger variation

480   of almost one order of magnitude and has a longer transitional period when compared to the

481   corresponding Nu and Sh. The short initial transient behavior of the transfer numbers is in

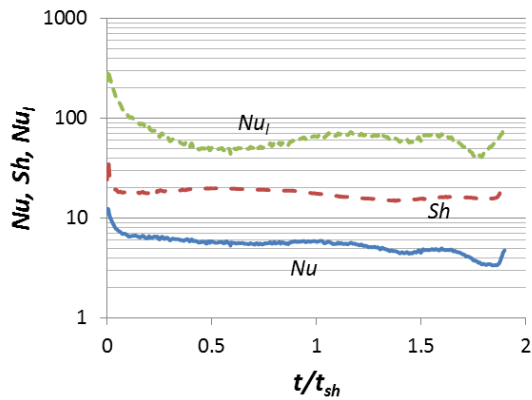482   agreement with the one calculated in [41, 42, 52].

483

484   Fig. 12: Temporal variation of Nu, Sh and Nu_l for the case of $(We,T)=(30,600)$.

485

486   Earlier CFD works on spherical droplet evaporation [41, 42] gave expressions of the Nu and Sh

487   numbers as a function of the instantaneous Re, Pr and Sc numbers. Nevertheless, this is not

488   applicable in the present work, since the duration of the phenomenon is short without any

489   appreciable changes of the droplet velocity and temperature. Thus, it was considered more

490   efficient to use time-averaged expressions based on the free-stream dimensionless numbers.

491   The time-averaged $\overline{Nu}$, $\overline{Sh}$ and $\overline{Nu_l}$ numbers are given in eq 11-13 and they can be used in

492   equations 8-10 instead of the corresponding instantaneous to predict the temporal evolution of

493   the droplet temperature and evaporation rate with sufficient accuracy; this is shown in Fig. 13

494   for two cases combining different *We* numbers and gas phase temperatures. As seen, the model

495   predictions for the average droplet temperature and the evaporation rate are satisfactory, while

496   for the surface temperature there are discrepancies due to the fact that Nu_l has a more transient

497   character, which is ignored when a time-averaged expression is used. Nevertheless, this

498   enhanced model is able to provide the additional information of surface temperature and

499   correctly predicts the trends of the evaporation rate and the average droplet temperature with

500   less than 0.5K error. For the surface temperature T_s, the initial condition used was to set it equal

501   to the contact temperature between semi-infinite solids [69] and this concept was also used in

502   [70-72] for droplet impact on hot substrates. The initial condition for the surface temperature is

503   shown in Equation 14 and agrees well with the CFD predictions at the first time-step.

$$T_{s,0} = \frac{\gamma_l T_0 + \gamma_g T_\infty}{\gamma_l + \gamma_g} \tag{14}$$
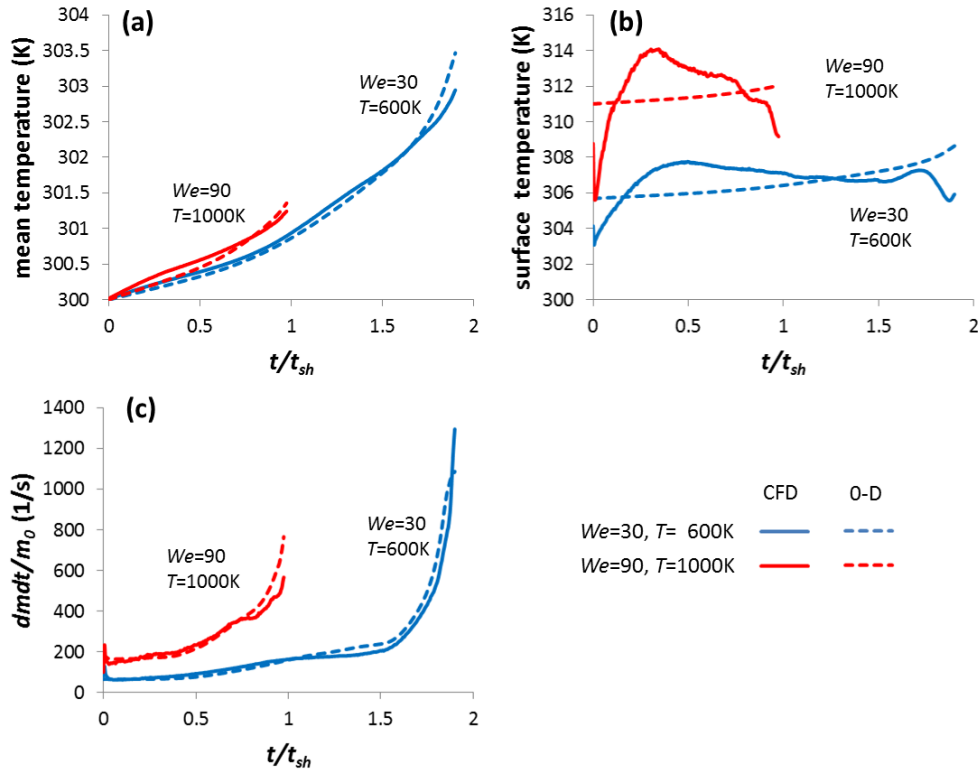
504

505

506

Fig. 13: Predictions of the 0-D model for (a) the volume averaged droplet temperature, (b) the
surface temperature and (c) the evaporation rate. Solid lines are the CFD data and dashed lines
are the 0-D model predictions.

510

Some further comments should be made for the set of equations 8-13. As the proposed
correlations represent time-average parameters, they are using the free-stream properties and
not film conditions, they are based on initial dimensionless numbers and do not account for
their temporal variation since the duration of the phenomenon is short. Under these
assumptions, the proposed correlations cannot be directly compared against others referring to
spherical droplets. Another limitation of the proposed 0D model, is that it requires the
knowledge of the temporal variation (history) of the droplet surface area. This can be done by
using Equation 3 for the temporal variation of the surface area, but more work is needed to
obtain the corresponding coefficients, since for the case of droplet evaporation they also depend

27

520 on the droplet heat-up. For the case in which the temporal evolution of the surface area is not

521 known, one can obtain qualitative but less accurate results, by using the surface area of a sphere

522 in Equations 8 and 9 and multiplying the $\overline{Nu}$ and $\overline{Sh}$ numbers with the correction factors

523 $\{1.28 + 0.7exp(-0.07|We - 30|)\}$ and $\{1.6 + 1.3exp(-0.07|We - 30|)\}$ respectively;

524 these are valid for supercritical ambient temperatures (T_∞>600K). A final comment should be

525 made for the equation describing the averaged Sh number (Equation 12), which was found to

526 be related with B_T and not the Spalding number B_M , since the initial droplet temperature and

527 the liquid species were fixed in the present work. Additionally, the Nu_l number in Equation 13

528 should be normally related to the liquid properties (e.g. the Pr_l number), but this is not

529 applicable in the present study since only one liquid species was examined. The Re_l appearing

530 in Equation 13 was taken from [73] and it is calculated as $Re_l = Re_\infty \varepsilon^{2/3} N^{-4/3}$.

531 Using the proposed 0-D model (equations 8-13) and the surface area variation according to

532 Equation 3 (extended up to the breakup instant and limited up to $S_{max}=10S_0$), one can estimate

533 initially the surface temperature at $t=t_{sh}$ and then the percentage change of the surface tension

534 coefficient σ, which has an important effect of the droplet heating; this is shown in Fig. 14, in

535 which the vertical axis values are presented in reversed order, and it is in agreement with the

536 corresponding CFD data at the same time instant. As seen, the relative change of surface tension

537 coefficient becomes important either for low We numbers or for high ambient temperatures, as

538 expected; it will not alter the breakup characteristics at high We cases. On the other hand, at the

539 low We number of 15 and T_∞=600K, the reduction of the surface tension coefficient by 3.5% is

540 enough to lead to breakup; note that in this specific case the droplet was not breaking up under

541 isothermal conditions. Finally, for a less volatile fuel than the examined n-heptane, the

542 reduction of surface tension coefficient is expected to be higher due to higher heating and this
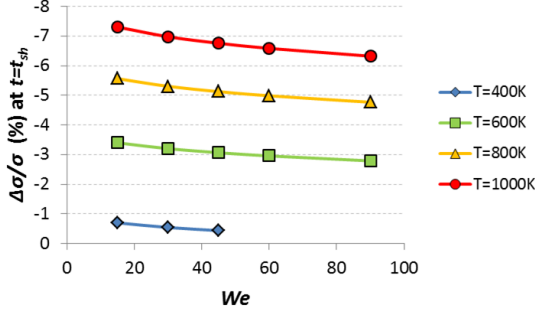
543 is a subject of future work.

544

545

Fig. 14: 0-D model predictions for the percentage change of surface tension coefficient at $t=t_{sh}$ as a function of *We* number and gas phase temperature.

548

Complimentary to the discussion about the reduction of the surface tension coefficient, the minor impact of droplet heating on the breakup of a volatile fuel droplet (except of the low *We* number cases) can be explained by comparing the associated timescales, either in a macroscopic or in a microscopic level. In a macroscopic level, the associated timescales are the shear breakup timescale t_{sh} and the thermal time constant $t_{thermal} = \rho_l c_{p,l} D_0^2 / \left(6 \, k_{g,\infty} \, \overline{Nu} \right)$. The latter can be deduced from Equation 8 (see also [69]) in which the surface area variation has been omitted for simplicity. At $t=0.1 t_{thermal}$ the temperature of a sphere will be $\sim 0.095(T_\infty \text{-} T_0)$, which can be a reasonable value for evaporating droplets, but still too high for droplet undergoing breakup. In any case, the ratio of these timescales ($0.1 t_{thermal}/t_{sh}$) is large (see Fig. 15a), implying that the droplet heating is a much slower process relative to the droplet breakup and it becomes less significant for high *We* numbers and high temperatures. In a microscopic level the associated timescales are the hydrodynamic timescale $t_{hydr,liq}=R^2/(\nu_l Re_l)$ (from [28] and Re_l from Equation 13) and the heat timescale of the liquid phase $t_{heat,liq}=R^2/a_l$, where a_l is the thermal diffusivity of the liquid phase. Their ratio is shown in Fig. 15b as a function of *We* number and gas phase temperature. This figure also verifies that heating plays a minor role since it is over 3 orders of magnitude slower than the momentum transport and becomes even less important for high *We*

29

565   cases. Other timescales examined based on gas phase properties and flow timescales (D/U)

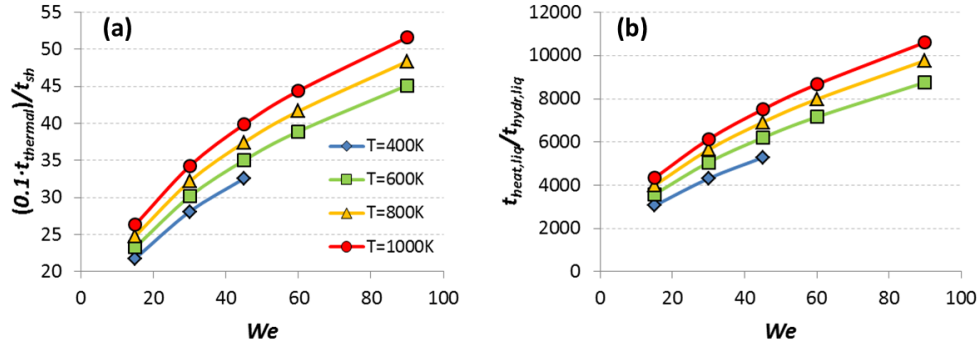566   have shown similar trends.

567

568

569   Fig. 15: Comparison of heating and flow timescales in (a) macroscopic and (b) microscopic

570   level as a function of We number and gas phase temperature.

571

3.3.3   Spatial distribution of flow variables

573   The spatial distribution of the droplet temperature and vapour concentration is shown in Fig.

574   16 for the case of $We=15$ and $T_\infty=600K$. In the front of the droplet, higher temperatures are

575   observed due to the hot oncoming flow. A very thin thermal boundary layer can be seen on the

576   inset figures in Fig. 16a, while at the rear of the droplet the thermal boundary layer is relatively

577   thicker affected by the internal liquid vortex which tends to transfer hot fluid from the hotter

578   surface towards the cooler inner droplet region. This confirms that the internal droplet

579   temperature distribution is mainly affected by convection rather than by conduction as stated

580   in Schlottke et al. [53]. The vapour concentration field shown in Fig. 16b is affected by the

581   recirculation zone in the gaseous phase and higher concentration values (except of the interface

582   region) are observed off-axis. A slightly different temperature field is observed in the high We

583   number case of 90 at the same gas temperature, which is shown in Fig. 17a. This time, the

30

584   mixing of temperature inside the liquid phase is almost absent due to the large difference

585   between the associated time-scales previously discussed, but also due to the fact that there are

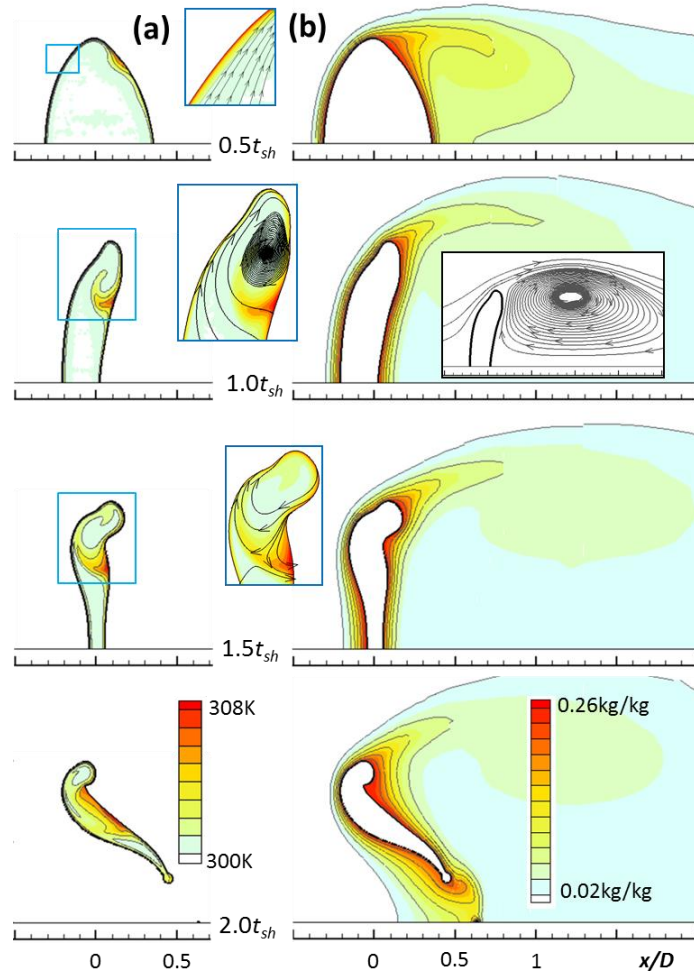586   no vortices inside the droplet.

587

588   Fig. 16: Spatial distribution of (a) droplet temperature and (b) vapour concentration for the case

589   (*We*, T_∞)= (15, 600). The inset figures aim to clarify the local relative velocity field.
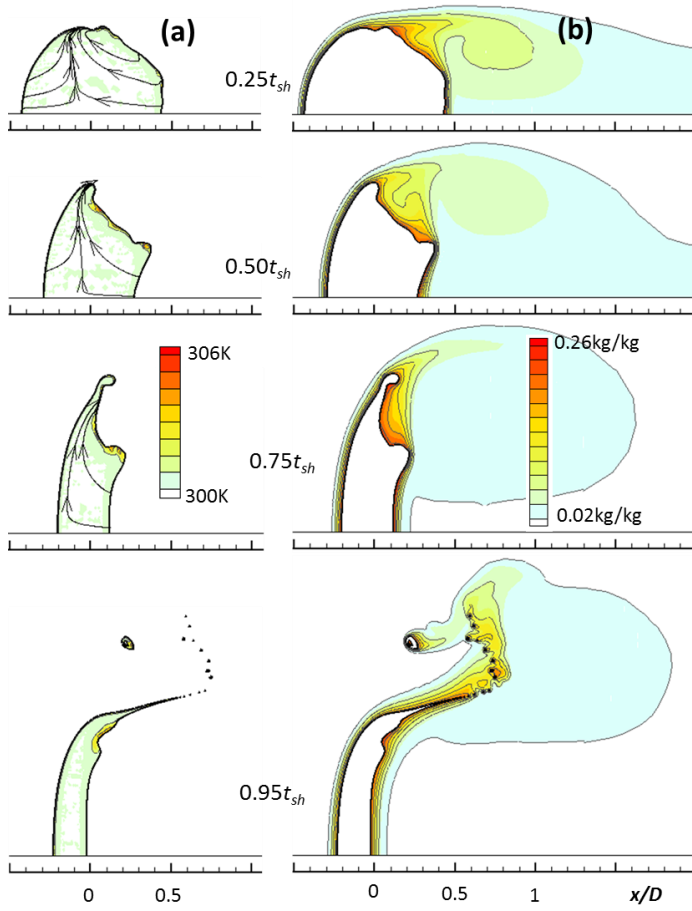
590

Fig. 17: Spatial distribution of (a) droplet temperature along with characteristic streamlines of the relative velocity field and (b) vapour concentration for the case (We, T_∞)= (90, 600).

4 Conclusions

A validated numerical model, which accounts for the Navier-Stokes equations coupled with the conservation of energy and species transport equations and the VOF methodology for capturing the gas-droplet interface, has been used to study the deformation and breakup of droplets at various We and Re numbers under either isothermal or evaporating conditions. The simulations verify that the We number is the controlling parameter defining the breakup outcome. For low We numbers there is a critical Re number that controls the occurrence of breakup. The numerical results obtained under isothermal conditions are in accordance with experimental observations

32

concerning the breakup time, the droplet deformation, the droplet velocity and the drag coefficient. When heating and evaporation are included, the surface tension coefficient decreases due to droplet heating, but the overall hydrodynamic behaviour is not remarkably changing, which is due to the short duration of the phenomenon relative to the heating timescale as also to the high volatility of the fuel examined which suppresses the droplet heat-up. Nevertheless, at low *We* numbers the associated timescales become closer and in combination with the large temperature difference between liquid and gas, the critical *Re* number for breakup becomes smaller. Relative to a spherical droplet, the increased liquid surface area due to the droplet deformation enhances the droplet heating and evaporation, but the evaporated mass is not exceeding 2% up to the instant of breakup.

By post-processing the CFD data for droplet heating and evaporation, an enhanced 0-D model is derived for a simple but still accurate estimation of droplet temperature and evaporation rate up to the breakup instant. Relative to classical 0-D models, the present one predicts also the surface temperature and it requires the knowledge of the surface area temporal evolution. Finally, the numerical predictions indicate that the spatial distribution of the vapour and temperature is affected by the vortices formed within the gas and the liquid phase. This is evident in the internal liquid temperature distribution for high *We* numbers, in which the absence of internal circulation leads to trapping the hot liquid near the interface.

5 Acknowledgements

627 # 6 Nomenclature

628 **Roman symbols**

Symbol	Description	Units
B	adjustable coefficient	-
B_M	Spalding number $B_M = (Y_s(T_s) - Y_\infty)/(1 - Y_s(T_s))$	-
B_T	Thermal Spalding number $B_{T,\infty} = c_{p,g,\infty}(T_\infty - T_0)/L$	-
C	Courant number $C = u \cdot \delta t/\delta x$	-
C_D	drag coefficient	-
c_p	Heat capacity	J/kgK
D	diameter	m
D_{AB}	Vapour diffusion coefficient	m^2/s
Oh	Ohnesorge number $Oh = \mu_l/\sqrt{\rho_l \sigma D_0}$	-
k	Thermal conductivity	W/mK
L	Latent heat of vaporization	J/kg
m	mass	kg
$\dot{m}''$	Evaporation rate per unit area	kg/m^{2}s
Nu	Nusselt number	-
p	pressure	Pa
Pe	Peclet number $Pe=Re \cdot Pr$	-
Pr	Prandtl number	-
R	radius	m
Re	Reynolds number $Re = \rho_g U_{rel,0} D_0/\mu_g$	-
S	surface area	m^2
Sc	Schmidt number	-
Sh	Sherwood number	-
t	time	s
t_{sh}	Shear breakup timescale $t_{sh} = D\sqrt{\varepsilon}/U$	-
T	temperature	K
U	reference velocity	m/s
u	instantaneous droplet velocity	m/s
V	volume	m^3
We	Weber number $We = \rho_g U_{rel,0}^2 D_0/\sigma$	-
We_t	instantaneous We number	-
X	droplet displacement	m
Y	vapour concentration	kg/kg

629
630
631 **Greek symbols**

Symbol	Description	Units
a	thermal diffusivity	m^2/s
γ	thermal effusivity $\gamma = \sqrt{k\rho c_p}$	J/m^{2}Ks$^{0.5}$

δt	timestep		s
δx	cell size		m
ε	density ratio $\varepsilon = \rho_l/\rho_g$		-
μ	viscosity		kg/ms
N	viscosity ratio $N = \mu_l/\mu_g$		-
v	kinematic viscosity		m^2/s
ρ	density		kg/m^3
σ	surface tension coefficient		N/m

632

Subscripts

Symbol	Description
0	initial
c	cross-stream
cr	critical
g	gas
l	liquid
rel	relative
s	at surface
t	instantaneous magnitude
x,y,z	coordinates
∞	free-stream conditions

633

Abbreviations

Symbol	Description
BFW	Body Force Weighted
BSOI	Bounded Second Order Implicit
CFD	Computational Fluid Dynamics
cpR	Cells per Radius
CSS	Continuum Surface Stress
FOU	First Order Upwind
PISO	Pressure-Implicit with Splitting of Operators
SOU	Second Order Upwind
UDF	User Defined Function

35

VOF   Volume of Fluid

634

References

636

[1] D.R. Guildenbecher, C. López-Rivera, P.E. Sojka, Secondary atomization, Experiments in Fluids, 46 (2009) 371-402.

[2] T.G. Theofanous, Aerobreakup of Newtonian and Viscoelastic Liquids, Annual Review of Fluid Mechanics, 43 (2011) 661-690.

[3] S.S. Sazhin, Advanced models of fuel droplet heating and evaporation, Progress in Energy and Combustion Science, 32 (2006) 162-214.

[4] H.Y. Erbil, Evaporation of pure liquid sessile and spherical suspended drops: A review, Advances in Colloid and Interface Science, 170 (2012) 67-86.

[5] R. Clift, J.R. Grace, M.E. Weber, Bubbles, drops and particles, Academic Press, New York, 1978.

[6] W.A. Sirignano, Fluid Dynamics and Transport of Droplets and Sprays, Cambridge University Press, 1999.

[7] Z. Liu, R.D. Reitz, An analysis of the distortion and breakup mechanisms of high speed liquid drops, International Journal of Multiphase Flow, 23 (1997) 631-650.

[8] C.H. Lee, R.D. Reitz, An experimental study of the effect of gas density on the distortion and breakup mechanism of drops in high speed gas stream, International Journal of Multiphase Flow, 26 (2000) 229-244.

[9] J.A. Nicholls, A.A. Ranger, Aerodynamic shattering of liquid drops, AIAA Journal, 7 (1969) 285-290.

[10] S.A. Krzeczkowski, Measurement of liquid droplet disintegration mechanisms, International Journal of Multiphase Flow, 6 (1980) 227-239.

[11] L.P. Hsiang, G.M. Faeth, Near-limit drop deformation and secondary breakup, International Journal of Multiphase Flow, 18 (1992) 635-652.

36

660   [12] L.P. Hsiang, G.M. Faeth, Drop properties after secondary breakup, International Journal
661   of Multiphase Flow, 19 (1993) 721-735.

662   [13] L.P. Hsiang, G.M. Faeth, Drop deformation and breakup due to shock wave and steady
663   disturbances, International Journal of Multiphase Flow, 21 (1995) 545-560.

664   [14] L. Opfer, I.V. Roisman, J. Venzmer, M. Klostermann, C. Tropea, Droplet-air collision
665   dynamics: Evolution of the film thickness, Physical Review E, 89 (2014) 013023.

666   [15] Z. Dai, G.M. Faeth, Temporal properties of secondary drop breakup in the multimode
667   breakup regime, International Journal of Multiphase Flow, 27 (2001) 217-236.

668   [16] X.-K. Cao, Z.-G. Sun, W.-F. Li, H.-F. Liu, Z.-H. Yu, A new breakup regime of liquid
669   drops identified in a continuous and uniform air jet flow, Physics of Fluids, 19 (2007) 057103.

670   [17] H. Zhao, H.-F. Liu, J.-L. Xu, W.-F. Li, K.-F. Lin, Temporal properties of secondary drop
671   breakup in the bag-stamen breakup regime, Physics of Fluids, 25 (2013) 054102.

672   [18] A.K. Flock, D.R. Guildenbecher, J. Chen, P.E. Sojka, H.J. Bauer, Experimental statistics
673   of droplet trajectory and air flow during aerodynamic fragmentation of liquid drops,
674   International Journal of Multiphase Flow, 47 (2012) 37-49.

675   [19] J. Han, G. Tryggvason, Secondary breakup of axisymmetric liquid drops. II. Impulsive
676   acceleration, Physics of Fluids, 13 (2001) 1554-1565.

677   [20] S. Khosla, C.E. Smith, Detailed Understanding of Drop Atomization by Gas Crossflow
678   Using the Volume of Fluid Method, in: ILASS Americas, Toronto, Canada, 2006.

679   [21] P. Khare, V. Yang, Drag Coefficients of Deforming and Fragmenting Liquid Droplets, in:
680   ILASS Americas, 2013.

681   [22] M. Jalaal, K. Mehravaran, Transient growth of droplet instabilities in a stream, Physics of
682   Fluids, 26 (2014) 012101.

683   [23] M. Jain, R.S. Prakash, G. Tomar, R.V. Ravikrishna, Secondary breakup of a drop at
684   moderate Weber numbers, Proceedings of the Royal Society of London A: Mathematical,
685   Physical and Engineering Sciences, 471 (2015).

686   [24] G.A.E. Godsave, Burning of Fuel Droplets in: 4th International Symposium on
687   combustion, The Combustion Institute, Baltimore, 1953, pp. 818-830.

688   [25] D.B. Spalding, The combustion of liquid fuels, in: 4th International Symposium on
689   combustion, The Combustion Institute, Baltimore, 1953, pp. 847-864.

690   [26] C.K. Law, Unsteady droplet combustion with droplet heating, Combustion and Flame, 26
691   (1976) 17-22.

692   [27] C.K. Law, W.A. Sirignano, Unsteady droplet combustion with droplet heating--II:
693   Conduction limit, Combustion and Flame, 28 (1977) 175-186.

694   [28] B. Abramzon, W.A. Sirignano, Droplet vaporization model for spray combustion
695   calculations, International Journal of Heat and Mass Transfer, 32 (1989) 1605-1618.

696   [29] M. Renksizbulut, M. Bussmann, X. Li, Droplet vaporization model for spray calculations,
697   Particle & Particle Systems Characterization, 9 (1992) 59-65.

698   [30] L.A. Dombrovsky, S.S. Sazhin, A parabolic temperature profile model for heating of
699   droplets, Journal of Heat Transfer, 125 (2003) 535-537.

700   [31] A.Y. Snegirev, Transient temperature gradient in a single-component vaporizing droplet,
701   International Journal of Heat and Mass Transfer, 65 (2013) 80-94.

702   [32] G.F. Yao, S.I. Abdel-Khalik, S.M. Ghiaasiaan, An Investigation of Simple Evaporation
703   Models Used in Spray Simulations, Journal of Heat Transfer, 125 (2003) 179-182.

704   [33] R.S. Miller, K. Harstad, J. Bellan, Evaluation of equilibrium and non-equilibrium
705   evaporation models for many-droplet gas-liquid flow simulations, International Journal of
706   Multiphase Flow, 24 (1998) 1025-1055.

707   [34] D.I. Kolaitis, M.A. Founti, A comparative study of numerical models for Eulerian-
708   Lagrangian simulations of turbulent evaporating sprays, International Journal of Heat and Fluid
709   Flow, 27 (2006) 424-435.

710   [35] S.S. Sazhin, T. Kristyadi, W.A. Abdelghaffar, M.R. Heikal, Models for fuel droplet heating
711   and evaporation: Comparative analysis, Fuel, 85 (2006) 1613-1630.

712   [36] Z. Zhifu, W. Guoxiang, C. Bin, G. Liejin, W. Yueshe, Evaluation of Evaporation Models
713   for Single Moving Droplet with a High Evaporation Rate, Powder Technology, 240 (2013) 95-
714   102.

715 [37] F. Mashayek, Dynamics of evaporating drops. Part I: formulation and evaporation model, International Journal of Heat and Mass Transfer, 44 (2001) 1517-1526.

717 [38] P. Tekasakul, S.K. Loyalka, Evaporation from non-spherical particles: the equivalent-volume and inscribed sphere approximations for nearly spherical particles, Journal of Aerosol Science, 33 (2002) 307-317.

720 [39] S. Tonini, G.E. Cossali, An exact solution of the mass transport equations for spheroidal evaporating drops, International Journal of Heat and Mass Transfer, 60 (2013) 236-240.

722 [40] S. Tonini, G.E. Cossali, An evaporation model for oscillating spheroidal drops, International Communications in Heat and Mass Transfer, 51 (2014) 18-24.

724 [41] R.J. Haywood, R. Nafziger, M. Renksizbulut, Detailed examination of gas and liquid phase transient processes in convective droplet evaporation, Journal of Heat Transfer, 111 (1989) 495-502.

727 [42] C.H. Chiang, M.S. Raju, W.A. Sirignano, Numerical analysis of convecting, vaporizing fuel droplet with variable properties, International Journal of Heat and Mass Transfer, 35 (1992) 1307-1324.

730 [43] A.T. Shih, C.M. Megaridis, Suspended droplet evaporation modeling in a laminar convective environment, Combustion and Flame, 102 (1995) 256-270.

732 [44] J. Schlottke, B. Weigand, Direct numerical simulation of evaporating droplets, Journal of Computational Physics, 227 (2008) 5215-5237.

734 [45] C.M. Megaridis, W.A. Sirignano, Multicomponent droplet vaporization in a laminar convective environment, Combustion science and technology, 87 (1992) 27-44.

736 [46] M. Renksizbulut, M. Bussmann, Multicomponent droplet evaporation at intermediate Reynolds numbers, International Journal of Heat and Mass Transfer, 36 (1993) 2827-2835.

738 [47] G. Strotos, M. Gavaises, A. Theodorakakos, G. Bergeles, Numerical investigation of the evaporation of two-component droplets, Fuel, 90 (2011) 1492-1507.

740 [48] R. Banerjee, Numerical investigation of evaporation of a single ethanol/iso-octane droplet, Fuel, 107 (2013) 724-739.

742 [49] R.J. Haywood, M. Renksizbulut, G.D. Raithby, Numerical solution of deforming
743 evaporating droplets at intermediate Reynolds numbers, Numerical Heat Transfer; Part A:
744 Applications, 26 (1994) 253-272.

745 [50] R.J. Haywood, M. Renksizbulut, G.D. Raithby, Transient deformation and evaporation of
746 droplets at intermediate Reynolds numbers, International Journal of Heat and Mass Transfer,
747 37 (1994) 1401-1409.

748 [51] Z.S. Mao, T. Li, J. Chen, Numerical simulation of steady and transient mass transfer to a
749 single drop dominated by external resistance, International Journal of Heat and Mass Transfer,
750 44 (2001) 1235-1247.

751 [52] M. Hase, B. Weigand, Transient heat transfer of deforming droplets at high Reynolds
752 numbers, International Journal of Numerical Methods for Heat & Fluid Flow, 14 (2003) 85 -
753 97.

754 [53] J. Schlottke, E. Dulger, B. Weigand, A VOF-based 3D numerical investigation of
755 evaporating, deformed droplets, Progress in Computational Fluid Dynamics, an International
756 Journal, 9 (2009) 426-435.

757 [54] R.F.L. Cerqueira, E.E. Paladino, C.R. Maliska, A computational study of the interfacial
758 heat or mass transfer in spherical and deformed fluid particles flowing at moderate Re numbers,
759 Chemical Engineering Science, 138 (2015) 741-759.

760 [55] R.H. Perry, D.W. Green, Perry's Chemical Engineers' Handbook, 7th ed., McGraw-Hill,
761 1997.

762 [56] B.E. Poling, J.M. Prausnitz, J.P. O'Connell, Properties of Gases and Liquids (5th Edition),
763 in, McGraw-Hill, 2001.

764 [57] G. Strotos, I. Malgarinos, N. Nikolopoulos, M. Gavaises, Predicting the evaporation rate
765 of stationary droplets with the VOF methodology for a wide range of ambient temperature
766 conditions, International Journal of Thermal Sciences, (under review) (2016).

767 [58] I. Malgarinos, N. Nikolopoulos, M. Gavaises, Coupling a local adaptive grid refinement
768 technique with an interface sharpening scheme for the simulation of two-phase flow and free-
769 surface flows using VOF methodology, Journal of Computational Physics, 300 (2015) 732-753.

770 [59] G. Strotos, I. Malgarinos, N. Nikolopoulos, K. Papadopoulos, A. Theodorakakos, M.
771 Gavaises, Performance of VOF methodology in predicting the deformation and breakup of
772 impulsively accelerated droplets in: 13th ICLASS, Tainan, Taiwan, 2015.

773 [60] G. Strotos, I. Malgarinos, N. Nikolopoulos, M. Gavaises, Predicting droplet deformation
774 and breakup for moderate Weber numbers, International Journal of Multiphase Flow, (under
775 review) (2016).

776 [61] I. Malgarinos, N. Nikolopoulos, M. Marengo, C. Antonini, M. Gavaises, VOF simulations
777 of the contact angle dynamics during the drop spreading: Standard models and a new wetting
778 force model, Advances in Colloid and Interface Science, 212 (2014) 1-20.

779 [62] ANSYS®FLUENT, Release 14.5, Theory Guide, in, 2012.

780 [63] A. Theodorakakos, G. Bergeles, Simulation of sharp gas–liquid interface using VOF
781 method and adaptive grid local refinement around the interface, International Journal for
782 Numerical Methods in Fluids, 45 (2004) 421-439.

783 [64] B. Lafaurie, C. Nardone, R. Scardovelli, S. Zaleski, G. Zanetti, Modelling Merging and
784 Fragmentation in Multiphase Flows with SURFER, Journal of Computational Physics, 113
785 (1994) 134-147.

786 [65] C. Aalburg, Deformation and breakup of round drop and nonturbulent liquid jets in
787 uniform crossflows, in: Aerospace Engineering and Scientic Computing, University of
788 Michigan, 2002.

789 [66] E.E. Michaelides, Particles, bubbles & drops: their motion, heat and mass transfer, World
790 Scientific, 2006.

791 [67] Z.-G. Feng, E.E. Michaelides, Drag Coefficients of Viscous Spheres at Intermediate and
792 High Reynolds Numbers, Journal of Fluids Engineering, 123 (2001) 841-849.

793 [68] M. Pilch, C. Erdman, Use of breakup time data and velocity history data to predict the
794 maximum size of stable fragments for acceleration-induced breakup of a liquid drop,
795 International Journal of Multiphase Flow, 13 (1987) 741-757.

796 [69] F.P. Incropera, D.P. de Witt, Fundamentals of Heat and Mass Transfer 3rd ed., Wiley, New
797 York, 1990.

798 [70] M. Seki, H. Kawamura, K. Sanokawa, Transient temperature profile of a hot wall due to
799 an impinging liquid droplet, Journal of Heat Transfer, 100 (1978) 167-169.

800 [71] G. Strotos, G. Aleksis, M. Gavaises, K.-S. Nikas, N. Nikolopoulos, A. Theodorakakos,
801 Non-dimensionalisation parameters for predicting the cooling effectiveness of droplets
802 impinging on moderate temperature solid surfaces, International Journal of Thermal Sciences,
803 50 (2011) 698-711.

804 [72] G. Strotos, N. Nikolopoulos, K.-S. Nikas, K. Moustris, Cooling effectiveness of droplets
805 at low Weber numbers: Effect of temperature, International Journal of Thermal Sciences, 72
806 (2013) 60-72.

807 [73] M. Renksizbulut, R.J. Haywood, Transient droplet evaporation with variable properties
808 and internal circulation at intermediate Reynolds numbers, International Journal of Multiphase
809 Flow, 14 (1988) 189-202.

810

811